The primary cosmic-ray energy spectrum measured with the Tunka-133 array

N.M. Budnev [b], A. Chiavassa [d], O.A. Gress [b], T.I. Gress [b], A.N. Dyachok [b], N.I. Karpov [a], N.N. Kalmykov [a], E.E. Korosteleva [a], V.A. Kozhin [a], L.A. Kuzmichev [a], B.K. Lubsandorzhiev [c], N.B. Lubsandorzhiev [a], R.R. Mirgazov [b], E.A. Osipova [a], M.I. Panasyuk [a], L.V. Pankov [b], E.G. Popova [a], V.V. Prosin [a,*], V.S. Ptuskin [f], Yu.A. Semeney [b], A.A. Silaev [a], A.A. Silaev(junior) [a], A.V. Skurikhin [a], C. Spiering [e], L.G. Sveshnikova [a], A.V. Zagorodnikov [b],

[a] *Skobeltsyn Institute of Nuclear Physics MSU, Moscow, Russian Federation*
[b] *Irkutsk State University, Irkutsk, Russian Federation*
[c] *Institute for Nuclear Research of the Russian Academy of Sciences, Russian Federation*
[d] *Dipartimento di Fisica dell'Universita and INFN, Torino, Italy*
[e] *DESY, Zeuthen, Germany*
[f] *IZMIRAN, Troitsk, Moscow Region, Russia*

Abstract

The EAS Cherenkov light array Tunka-133, with ~ 3 km^2 geometric area, is taking data since 2009.The array permits a detailed study of energy spectrum and mass composition of cosmic rays in the energy range from $6 \cdot 10^{15}$ to 10^{18} eV. We describe the methods of time and amplitude calibration of the array and the methods of EAS parameters reconstruction. We present the all-particle energy spectrum, based on 7 seasons of operation.

Key words: High energy cosmic rays; air shower; Cherenkov radiation; energy spectrum

1. Introduction

The study of energy spectrum and mass composition of primary cosmic rays in the energy range of 10^{15} - 10^{18} eV is of crucial importance for understanding origin and propagation of cosmic rays (CR) in the Galaxy. An increasing dominance of heavy nuclei from the "knee" up to 10^{17} eV indicates the energy limit of CR acceleration in the standard model of particle acceleration in supernova remnants, see review [1]. At higher energies, the composition becomes lighter again up to $2 \cdot 10^{18}$ eV. This may indicate a transition to an extragalactic origin of CR or the dominance of new Galactic sources of unknown nature, see [2] for discussion.

To measure the primary energy spectrum and mass composition of cosmic rays in the energy range mentioned above, the Tunka-133 array [3,4] with nearly 3 km^2 geometrical area has been deployed in the Tunka Valley, Siberia. It records the Cherenkov light from Extensive Air Showers (EAS) using the Earth atmosphere as a huge calorimeter.

* Corresponding author.
Email address: v-prosin@yandex.ru (V.V. Prosin).

2. The Tunka-133 Array

The Tunka-133 array is located at an altitude of 670 m a.s.l. It consists of 175 optical detectors. The detectors are grouped into 25 clusters with seven detectors each – six hexagonally arranged detectors and one in the center. The distance between the detectors in a cluster is 85 m (see Fig. 1). 19 of the clusters are arranged as a dense central part of the array with a radius of about 500 m. These $19 \times 7 = 133$ stations gave the array its name. The remaining clusters are installed at distances of ≈ 1 km around the central part.

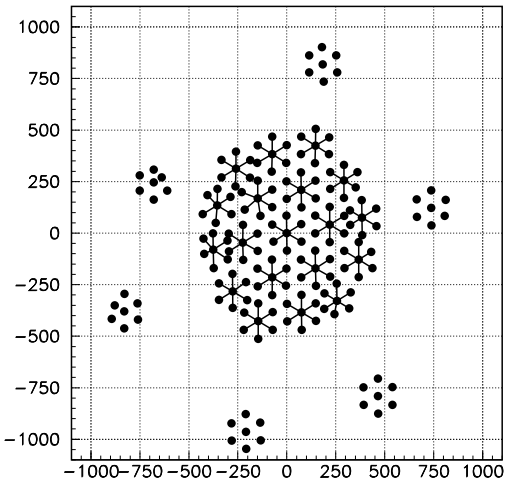

Fig. 1. Layout of the Tunka-133 array.

Each optical detector consists of a metallic cylinder with 50 cm diameter, containing a single PMT with a hemispherical photocathode of 20 cm. The container window consists of plexiglass and points vertically upward. It is heated against hoar-frost and dew. The detector is equipped with a remotely controlled lid protecting the PMT from daylight and precipitation.

Figure 2 shows the detector acceptance as a function of the zenith angle. The curve reflects the influence of the window edge as well as the atmosphere absorption due to Rayleigh and aerosol scattering of the Cherenkov light. To check the simulated detector acceptance we analyse the zenith angle distribution of the recorded EAS with reconstructed energies larger than 10.0 PeV. The resulting zenith angle distribution is shown in Fig. 3. The distribution is flat up to 50°.

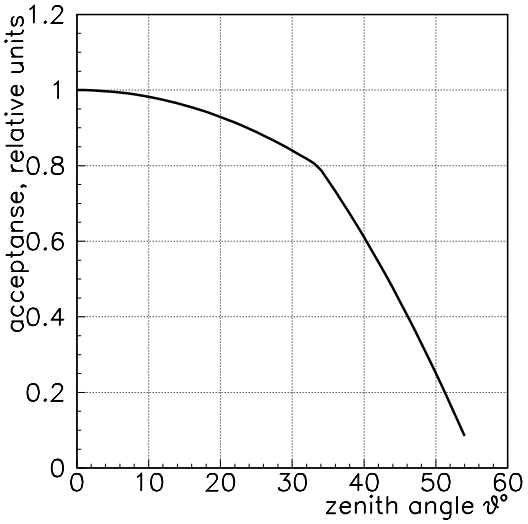

Fig. 2. Acceptance of the optical detector vs. zenith angle.

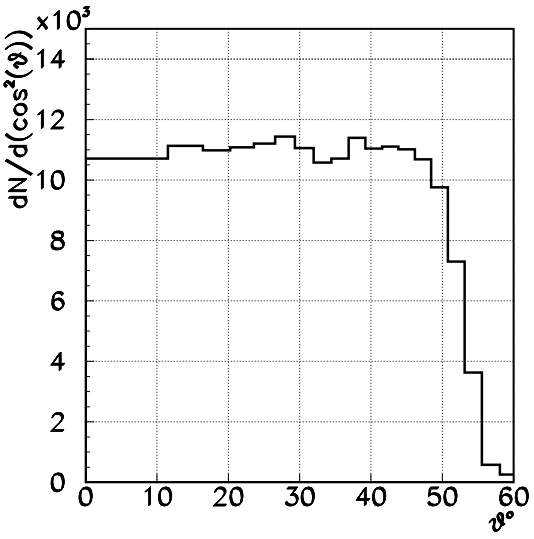

Fig. 3. Zenith angle distribution of showers with a reconstructed energy larger than 15.0 PeV.

The PMT pulses are amplified by pre-amplifiers and sent via 95 m coaxial cables RG58 to the electronics box in the center of each cluster and digitized there. The digital information is stored in the cycle buffer memory. The memory is stopped, and the data is sent to the central DAQ system in case of a cluster trigger appearence. The trigger condition is the appearence of pulses exceeding the digital threshold (see apparatus description [5]) at 3 or more detectors of a cluster within a time gate of 0.5 μs.

The minimum pulse width is about 20 ns. The dynamic range of the amplitude measurement is about $3 \cdot 10^4$. This is achieved by means of two channels for each detector extracting the signals from the anode and an intermediate dynode of the PMT with different additional amplification factors.

The data of all clusters is collected by the central DAQ and transferred via fiber-optics cables.

The amplitude calibration of the detectors was carried out in two steps similar to that used at the previous experiment Tunka-25. The details are described in [6].

3. Calibration

3.1. *Timing calibration*

The timing calibration of the detectors is performed using the experimental data from the recorded air showers.

The calibration inside a single cluster consists of a multiple reconstruction of zenith angle θ and azimuth angle ϕ for all the recorded showers, with an analysis of the residual difference between the measured and the theoretically expected delay for 6 peripheral detectors of a cluster. For calibration purposes at this step we use a plane model of the shower front. Modelling a curved shower front demands knowledge of the EAS core position which we reconstruct only at later steps. The difference between plane front and a realistic curved front leads to a larger dispersion of the residuals ΔT_i but it does not distort very much the mean value of ΔT_i ($\langle \Delta T_i \rangle$) because of an almost uniform core distribution across a cluster area and the limited size of the clusters.

The residual $\langle \Delta T_i \rangle$ is treated as an additional apparatus shift and added to the calibration shift. Then the procedure of the arrival direction reconstruction is repeated several times till all the detector shifts become less than $\langle \Delta T_i \rangle = 1$ ns.

The obtained corrections of time shifts are used for a preliminary reconstruction of the EAS core position with a plane model of the shower front, using that single cluster which recorded the largest amplitudes of pulses.

At the second step of the timing calibration we select large showers with more than 8 hit clusters and reconstruct the shower front assuming a curved shape derived from CORSIKA simulations and described in the next section.

The space basement of optical stations for such events is more than 500 m. Therefore the error of cluster synchronization (about 10 ns) leads to a maximum error in the arrival direction of 0.4°.

Finally the two calibration parameters are *a)* the delays between the central stations of the different clusters and *b)* the delays of the peripheral detectors within a cluster relatively to their central one.

The corrections of the central station delays are obtained applying the multi-cluster procedure for the central stations only to a single cluster, one but with a curved shape of the shower front.

The last correction of the time shifts is made synchronously for all 6 peripheral detectors of a cluster rotating their common plane so that the EAS axis direction measured by each single cluster coincides with the direction derived from a multi-cluster reconstruction with an accuracy better than 0.5°. An example of an EAS front reconstructed after the time calibration procedure is presented in Fig. 4.

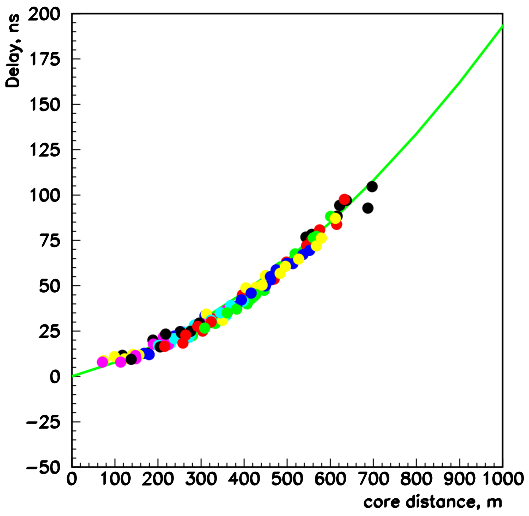

Fig. 4. An EAS front reconstructed from an experimental event, $E_0 = 6.8 \times 10^{17}$ eV, zenith angle $\theta = 19.2°$

3.2. *Relative amplitude calibration*

The amplitude calibration of the detectors was carried out in two steps [6]. The first step is a relative calibration, i.e. a derivation of the amplitude alignment coefficients for all individual detector outputs when the optical detectors were illuminated by the same light flashes.

Differences in gain and quantum efficiency of individual detectors resulted in output signal amplitude variations of a factor 2-3.

As the apertures of all detectors are the same, these coefficients were determined by comparing the amplitude spectra of the EAS Cherenkov light flashes. The residual dispersion after the renormalizing was less than 10%. Due to the stability of the EAS flux, the variation of the coefficient essentially reflects the time drift of the PMT gain as well as the relative atmospheric transparency.

The second step was the absolute calibration, made by normalization of the obtained integral energy spectrum to a reference spectrum. The details of this procedure will be described in section 4.5.

4. EAS parameter reconstruction

4.1. *Fitting the Cherenkov light pulse*

The raw data record for each Cherenkov light detector contains 1024 amplitude values a_k in steps of 5 ns (Fig. 5). Thus each pulse waveform is recorded over 5 μs.

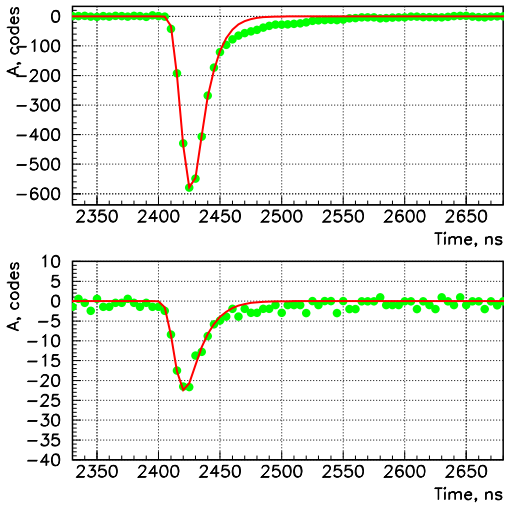

Fig. 5. Experimentally recorded pulses. The upper panel displays a pulse from the high gain channel (anode), the lower panel displays the same pulse recorded with a low gain channel (dynode). Each curve is a fit of the experimental points by expression (1).

The waveform of the light pulse is too complicated to be fitted with any simple function like a Gaussian or gamma function. We have constructed a function which separately approximates front and tail of a pulse [7]. The expression is based on 4 independent variables: the pulse amplitude A, the time of the pulse maximum t_{max}, and t_{front} and t_{tail} – the times of the front (pulse reaching 0.1 A) and the tail (pulse falling to 0.1 A).

From these variables we derive:

$$x = t - t_{max}$$
$$f = |x/t_{front}|$$
$$g = x/t_{tail}$$
$$h = \begin{cases} 1.7 - 0.5 \cdot g, & \text{if} \quad g < 0.8 \\ 1.3, & \text{if} \quad g \geq 0.8 \end{cases}$$

Using these variables the function for fitting the pulse waveform is as follows:

$$a(t) = \begin{cases} A \cdot \exp(-f^{2+0.5 \cdot f}), & \text{if} \quad x \leq 0 \\ A \cdot \exp(-g^h), & \text{if} \quad x > 0 \end{cases} \qquad (1)$$

This expression reasonably well approximates the pulse waveform from the level of $0.1A$ at the front edge to the level of $0.2A$ at the droop of the pulse. This time range is enough to determine by fitting function (1) such pulse parameters as peak amplitude A_i and front delay t_i at the level of $0.25 \cdot A_i$. The pulse area Q_i is measured by digital integration of the waveform starting from the level $0.05 \cdot A_i$ at the front till the same level at the tail. A fourth pulse parameter is the effective width $\tau_{eff} = Q_i/(1.24 \cdot A_i)$. The accuracy of this parameter is better than that of the pulse width (FWHM) used in earlier reports.

An example of a fit of experimental pulses with expression (1) is shown in Fig. 5.

4.2. *Arrival direction*

Zenith angle θ and azimuth angle ϕ of the shower direction are reconstructed by fitting the measured delays with the curve shower front: $\Delta T = T_i - T_f = R \cdot (R + 500)/(c \cdot F)$, where T_f is the estimated delay for a plane front, R the perpendicular distance from the shower axis in meters, c the speed of light and F the third variable parameter (together with θ and ϕ). This approximation is derived from the analysis of simulated showers with CORSIKA. The formula, on the one hand, has a non-zero value of the derivative at $R = 0$ (conical shape, typical for Cherenkov radiation at short distances from the axis) and on the other hand, has only one shape parameter which

is essential for processing of relatively small showers. To obtain R one needs to know the EAS core position.

4.3. *Core position*

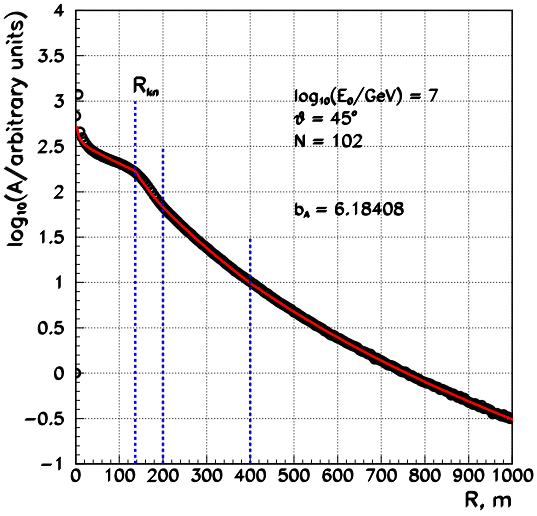

Fig. 6. An example of the ADF of a simulated event fitted with expression 3.

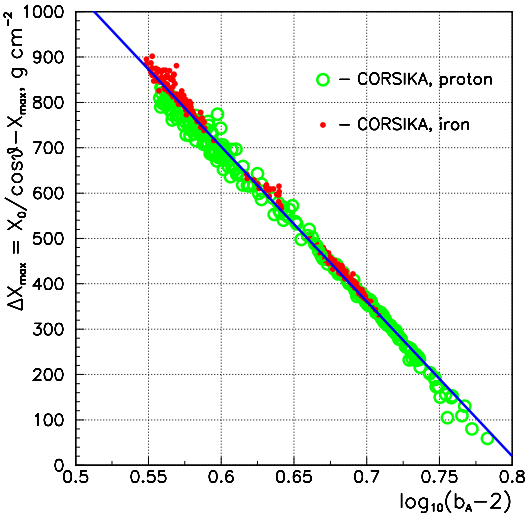

Fig. 7. Correlation between b_A and the thickness of matter between observational level and the EAS maximum depth.

The reconstruction of the EAS core position is performed by fitting the measured amplitudes A_i with an amplitude distance function (ADF):

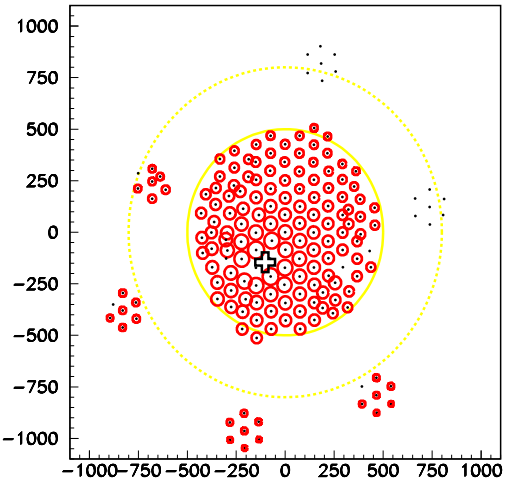

Fig. 8. Example of an experimental EAS core reconstruction. The radius of each station circle is proportional to $\log Q_i$. The cross marks the reconstructed position of the shower core.

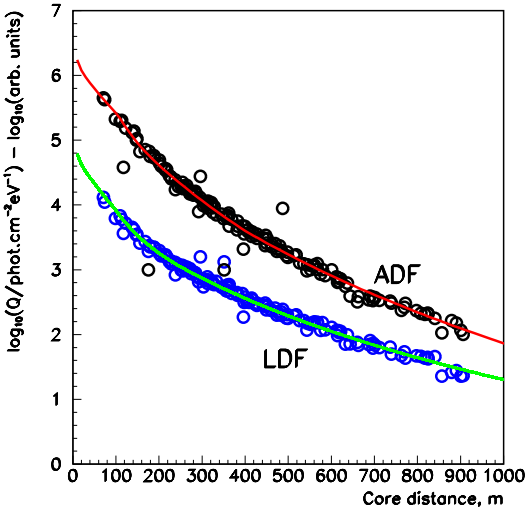

Fig. 9. Pulse amplitudes of the event shown in Fig. 6. Upper curve: fitted with ADF (expression 3, arbitary units). Lower curve: fitted with LDF (expression 6).

$$A(R) = A(200) \cdot p(R), \qquad (2)$$

The shape of the ADF was been studied with CORSIKA simulated events. It has been checked for simulated events in the energy range $10^{15} - 10^{18}$ eV, for primary protons and iron nuclei, and for zenith angles from 0° to 45°. It cannot be fitted with any simple function. Therefore we have desinged a func-

tion consiting of four different parametrizations for four different distance ranges (see [8]).

The first one closest to the core is an exponential function with variable parameter R_0 and addition of a pole close to $R = 0\,\mathrm{m}$. This parametrization is changed to a power law function at the variable distance marked as "knee" (R_{kn}). The index of the power law b is also variable. This function is changed to a Linsley function with a variable parameter a at the distance range 200 - 400 m. The last parametrization is the same function with fixed value of $a = 1$. The function $p(R)$ is a fit to four different parametrizations with respect to the distance R to the shower core (in meters):

$$p(R) = \begin{cases} \exp\left(\dfrac{(R_{\mathrm{kn}} - R)}{R_0}\left(1 + \dfrac{3}{R+2}\right)\right), \\ \qquad R < R_{\mathrm{kn}} \\ \left(\dfrac{200}{R}\right)^{b}, \qquad R_{\mathrm{kn}} \le R \le 200\,\mathrm{m} \\ \left(\left(\dfrac{R}{200} + a\right)/(1+a)\right)^{-b_A}, \\ \qquad 200\,\mathrm{m} \le R \le 400\,\mathrm{m} \\ \left(\left(\dfrac{R}{200} + 1\right)/2\right)^{-b_A}, \\ \qquad R > 400\,\mathrm{m} \end{cases} \tag{3}$$

All four variables in equation (3) (R_0, R_{kn}, a and b), describing the ADF shape in different ranges of core distance R are related to a single parameter of the ADF shape – the steepness b_A:

$$\begin{aligned} d &= b_A - 5 \\ D &= \log_{10}(d), \\ R_0 &= 275/d^2, \\ R_{\mathrm{kn}} &= 145 - 115 \cdot D, \\ a &= 0.89 - 0.29 \cdot D, \\ b &= \begin{cases} 2.4 + 2 \cdot (D - 0.15), & b_A \ge 6.41 \\ 2.4, & b_A < 6.41 \end{cases} \end{aligned} \tag{4}$$

The ADF steepness parameter b_A is treated as an independent variable during the minimization procedure. If, however, the core position is far from the dense parts of the array, b_A is treated as a fixed parameter. In this case it's value is derived from the value of X_{max}, obtained in turn from the mean width τ_{eff} of Cherenkov light pulses at a distance of $R = 400\,\mathrm{m}$. The connection relation τ_{eff} vs. X_{max} and b_A vs. X_{max} has been obtained and discussed in [8].

An example of CORSIKA simulated ADF fitted with formula (3) is shown in Fig. 6. Figure 7 presents the result of fitting some hundreds of simulated events for different zenith angles, different energies and different sorts of nuclei listed above as the correlation between b_A and the thickness of matter between the EAS maximum and the array. An example of core reconstruction is presented in Fig. 8. The appropriate functions ADF (3) and LDF (see expression (6) below) for this event are presented in Fig. 9.

4.4. *Energy reconstruction*

As a measure of energy we use the light flux density at a distance $R = 200\,\mathrm{m}$ – $Q(200)$. Reconstruction of $Q(200)$ is made by fitting the measured values of Q_i with the lateral distribution function (LDF). The new expression used now differs slightly from our previous version described in [9].

$$Q(R) = Q(200) \cdot q(R), \tag{5}$$

The function $q(R)$ is a combination of three different parametrizations according to the distance R to the shower core (in meters):

$$q(R) = \begin{cases} \left(\dfrac{200}{R_{\mathrm{kn}}}\right)^{b_2} \cdot \exp\left(\dfrac{R_{\mathrm{kn}} - R}{R_0}\left(1 + \dfrac{3}{R+3}\right)\right), \\ \qquad R < R_{\mathrm{kn}} \\ \left(\dfrac{200}{R}\right)^{b_2}, \qquad R_{\mathrm{kn}} \le R \le 300\,\mathrm{m} \\ \left(\dfrac{2}{3}\right)^{b_2} \cdot \left(\left(\dfrac{R}{300} + 1\right)/2\right)^{-b_Q}, \\ \qquad R > 300\,\mathrm{m} \end{cases} \tag{6}$$

All three variables in equation (3) (R_0, R_{kn} and b_2), describing the LDF shape in the different ranges of core distance R are related to a single parameter of the LDF shape – the steepness b_Q:

$$\begin{aligned} R_0 &= 200 \cdot (b_Q - 2.6)^{1.76}, \\ R_{\mathrm{kn}} &= 100 + 38 \cdot (b_Q - 4.5)^2, \qquad b_Q \le 4.5 \\ R_{\mathrm{kn}} &= 100, \qquad\qquad\qquad\quad b_Q > 4.5 \\ b_2 &= 1.97 + 0.12 \cdot (b_Q - 3.314)^2 \end{aligned} \tag{7}$$

The connection between the EAS energy E_0 and $Q(200)$ has been obtained from CORSIKA simula-

tions. The result of the simulation using QGSJET-II-04 is shown in Fig. 10. Black points are the mean values of $Q(200)$ for primary protons, red points are the mean values of $Q(200)$ for primary iron nuclei. The simulation was made for discrete energies 3, 10, 30, 100, 300, 1000, 3000 and 10000 PeV and zenith angles 30° and 45°. A simplified primary composition was supposed, consisting of equal contributions of protons and iron nuclei ($\ln A = 2.0$), for energies $\leq 3 \cdot 10^{17}$ eV. The pure proton composition is supposed for the energy 10^{18} eV in accordance with the results of TA [10] and PAO [11] experiments.

A linear fit of the individual simulated points gives

$$\log_{10}(E_0) = C_A + (0.940 \pm 0.003) \cdot \log_{10}(Q(200)), \quad (8)$$

for fitting over the energy range $3 \cdot 10^{15} - 10^{17}$ eV and

$$\log_{10}(E_0) = C_B + (0.951 \pm 0.002) \cdot \log_{10}(Q(200)), \quad (9)$$

for fitting over the energy range $10^{17} - 10^{18}$ eV.

The constant C_A is obtained from the procedure of absolute energy calibration (by the normalization to the reference CR integral intensity) described at the next subsection. The constant C_B can be obtained from C_A and the expressions (8) and (9):

$$C_B = (0.951 \cdot C_A - 0.01 \cdot 17)/0.940, \quad (10)$$

We have analyzed a possible influence of the uncertainty in composition to the calculation of E_0 from $Q(200)$. Changing the iron percentage in the composition from 30 % to 70 % changes $\ln A$ from 1.2 to 2.8 and the value of the coefficients at the expressions (8) and (9) by less than ± 0.01. This is one of the sources of the systematic uncertainty in the absolute energy estimation.

4.5. *Absolute energy calibration*

To reconstruct the EAS primary energy from the Cherenkov light flux measurements one needs to know the absolute sensitivities of the Cherenkov detectors and the atmosphere transparency. To avoid these problems, the method of normalization of the integral energy spectrum to a reference spectrum is used. The reference energy spectrum was measured by the QUEST experiment [12], [13]. The procedure of the normalization starts by the precise measurement of the EAS (or the primary particle) integral flux for the measured codes (or the relative energy). To measure the integral flux the number of events exceeding a measured relative code is calculated. The

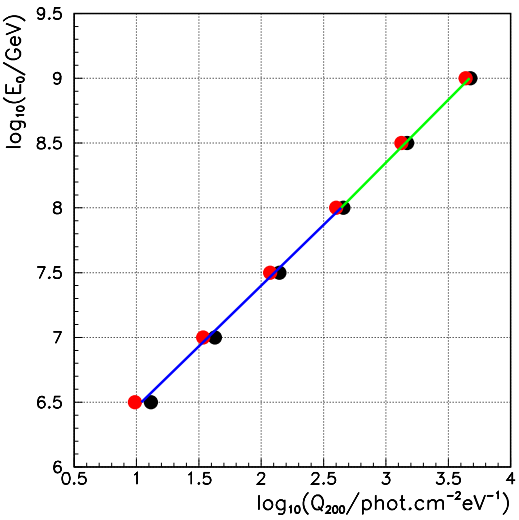

Fig. 10. CORSIKA QGSJET-II-04 simulation of $Q(200)$ vs. E_0. Black points are the mean values of $Q(200)$ for primary protons, red points are the mean values of $Q(200)$ for primary iron nuclei.

integral flux is obtained by dividing this number by the selected effective area, the selected effective solid angle and the observation time. The so obtained (for each night of Tunka-133 operation) integral energy spectrum is compared at the fixed flux level with the reference spectrum point. This comparison provides the normalisation constant C_A in expressions (8), used for calculation of the absolute primary particle energy of all the events independently of their EAS core position.

The exact point for normalization is chosen depending on the threshold of the experiment, because it has to have the maximal possible statistics for the events, registered with the efficiency close to 100%. It was $3 \cdot 10^{15}$ eV for the Tunka-25 array [6] where different PMTs (QUASAR-370) with about 4 times larger photocathode area were used. The normalization energy point for the first 3 years of Tunka-133 operation was estimated as $6 \cdot 10^{15}$ eV. About 5 years ago the authorities of the nearest villages (situated 3 km from the array site) installed new street lights much brighter than the previous ones, so the level of artificial light background became much higher. Therefore we used a normalization energy of 10^{16} eV for the last 4 years.

The systematic uncertainty in the reconstructed primary energy was estimated in Ref. [13] to be less than 10%.

This systematic error together with the above

mentioned uncertainty (±0.01) in the coefficients (0.940 and 0.951) in formulae 8 and 9 provides the systematic uncertainty in the primary energy spectrum which will be shown in Fig. 15.

4.6. *Experimental evaluation of the accuracy of the main EAS parameters*

The accuracy of the reconstructed shower parameters can be estimated using the well known chessboard method [14]. To use this method, the array is divided into two independent sub-arrays of similar size and configuration. Then the EAS parameters are derived independently with each of the two sub-arrays. The accuracy of any parameter is given by the difference between the two reconstructed values divided by a factor of $\sqrt{2}$ because they represent two independent experimental determinations of the same shower parameter. Applying this method to the Tunka-133 data, we composed the first sub-array from detectors with odd station IDs and the second one from detectors with even station IDs. The results are shown in Figs 11 and 12.

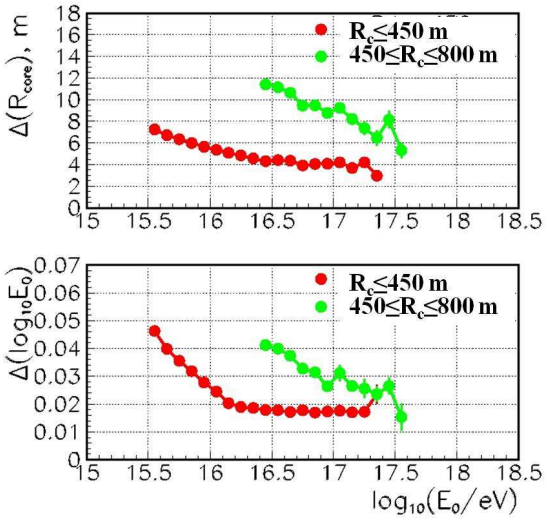

Fig. 11. Upper panel – errors of core position reconstruction. Lower panel – relative errors of primary energy reconstruction.

The upper panel of Fig. 11 shows the errors of the reconstruction of the core position R_c. In the central part of the array ($R_c \leq 450\,\mathrm{m}$) where showers with $\log_{10} E_0 \geq 15.5$ are recorded with almost 100% efficiency (see section 5), the error in R_c is less than 8 m. For the outer, sparsely instrumented region

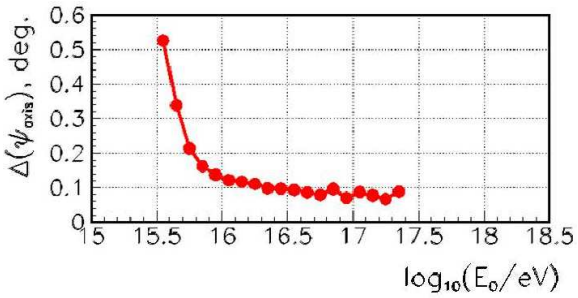

Fig. 12. Error of arrival direction.

($450\,\mathrm{m} \leq R_c \leq 800\,\mathrm{m}$) a 100% efficency is reached only for $\log_{10} E_0 \geq 16.5$ with an error in R_c almost twice of that for the inner region. The lower panel of Fig. 11 shows the relative uncertaintly in the primary energy E_0. For the central part of the array, the error in $\log_{10} E_0$ decreases rapidly from 0.05 at $\log_{10} E_0 \sim 15.5$ to 0.02 for $\log_{10} E_0 > 16.0$. Even for events with their core in the peripheral regions and $\log_{10} E_0 > 16.5$, the error is smaller than 0.04. These values are much smaller than the binning of our energy spectra ($\Delta_{bin} \log_{10} E_0 = 0.1$) avoiding a spectral deconvolution of the latter. Fig. 12 shows the error of the arrival direction. For $\log_{10} E_0 \geq 16$, it becomes smaller than 0.12°.

5. Energy spectrum

5.1. *Experimental data*

Tunka-133 operates in clear moonless nights from October to early April. During the other months, the nights are too short for economical operation and the weather conditions are mostly unsatisfactory. Here we present the data from 7 seasons. The total operation time with good weather conditions is 2175 hrs. The mean trigger rate is about 2 Hz. The number of recorded events is $\sim 1.4 \cdot 10^7$.

To reconstruct the differential energy spectrum the number of events inside each bin of 0.1 in $\log E_0$ is calculated. The differential uncorrected intensity (I_{uc}) is obtained by dividing this number by the selected effective area, the selected effective solid angle, the observation time and the energy bin width. We have selected events with zenith angles $\theta \leq 45°$.

Fig. 13 shows I_{uc} for the very dense array Tunka-25 [6], for the dense inner part of Tunka-133 ($R_c < 450\,\mathrm{m}$) and for full Tunka-133 ($R_c < 800\,\mathrm{m}$). Tunka-25 had a much lower energy threshold than Tunka-133 (it is $\sim 100\%$ efficient for $\log_{10} E_0 \geq 15$)

and can be used to experimetally derive the Tunka-133 efficiency in the overlapping region. One sees that for the inner region ($R_c \leq 450$ m, red dots) full efficiency is reached at $\log_{10} E_0 \sim 15.7$ while for the full array, i.e. adding the outer sparsely intrumented regions with 450 m $\leq R_c \leq 80$ m (blue dots) it is reached only at $\log_{10} E_0 \sim 16.7$. In the outer regions the condition for a shower to be recorded was chosen to be two or more hit clusters, since for a single-cluster event there is no measurement of the Cherenkov light flux at a core distance 200 m, whis is used for the energy evaluation.

The Monte-Carlo-calulated efficiency of the inner part of Tunka-133 ($R_c \leq 450$ m) as a function of shower energy is shown in Figure 14 as the ratio of the number of recorded events to the number of generated events. At $\log_{10} E_0 \sim 15.35$ the MC calulated efficiency (curve) is ~ 50 % and rises to an almost constant value of 95-100% for $\log_{10} E_0 \geq 15.8$, in accordance with the efficiencies derived from the uncorrected intensities shown at Figure 13 (red dots). The decreasing efficiency of I_{uc} for $\log_{10} E_0 < 15.8$ is due to the fact that below this energy showers are less efficiently recorded even in the inner, densely instumented part.

To reconstruct the spectrum for $\log_{10} E_0 < 17$ (where we are not limited by statistics) we used only events with $R_c \leq 450$ m, since they have more hits and consequently a better quality than events with the same energy but $R_c \geq 450$ m. For $\log_{10} E_0 > 17$ (where according to Fig. 13 also the full array is 100% efficient) we used all events with $R_c < 800$ m. For the highest points of the spectrum, with progressively low statistics, we doubled the bin size from 0.1 to 0.2 in $\log_{10} E_0$. The number of events with $R_c \leq 800$ m and $\log_{10} E_0 \geq 17$ is 4224.

Due an increasing level of light from artificial sources in a nearby village, we had to raise our triggering theshold after the first three years. This affects only the first two points of the spectrum. For the reconstruction of these two points we therefore use only data from the first 3 years of operation.

The resulting differential energy spectrum is shown in Fig. 15 together with the previous spectrum of Tunka-25 [6]. This and the following figures of course show the points with efficiency close to 100% according to Fig. 13 and Fig. 14.

The green contours bracket the possible systematic errors (described above in the section 4.5) due to the absolute normalisation procedure and - to a lesser degree - to the uncertainty of the coefficients (0.940 and 0.951) in expressions (8) and (9), connected with the above mentioned uncertainty in the mass composition. A digital representation of the spectrum is presented in Table 1 together with the number of events, statistical and systematic errors.

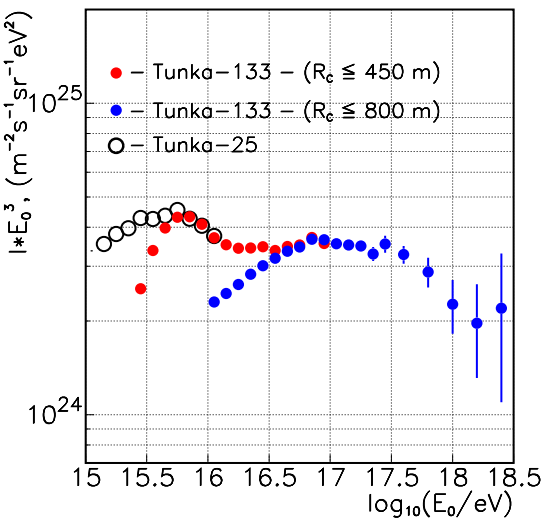

Fig. 13. Differential primary cosmic-ray intesity (uncorrected for registration efficiency) I_{uc} for two collecting areas: $R_C \leq 450$ m and $R_C \leq 800$ m – before combining.

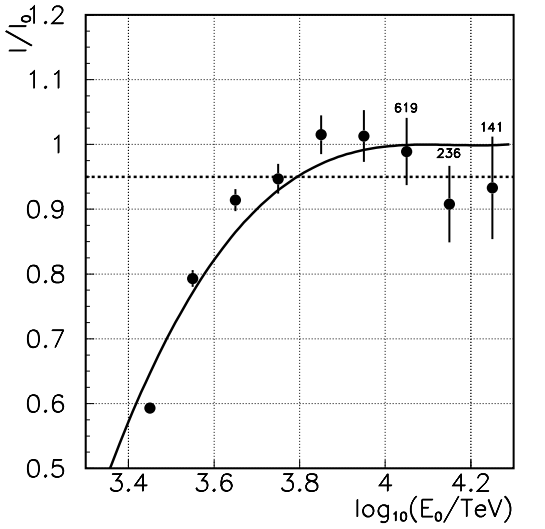

Fig. 14. Energy dependence of the EAS registration efficiency in the threshold energy range. Points are the experimental estimation from Tunka-25 and Tunka-133 data comparison, the solid line is a result of simulation, the dotted line is the efficiency level for the events used for the spectrum reconstruction.

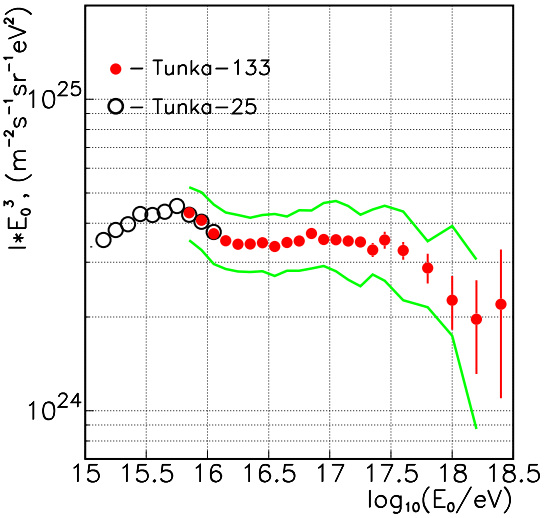

Fig. 15. Differential primary cosmic-ray energy spectrum. Green contours bracket the possible systematic errors.

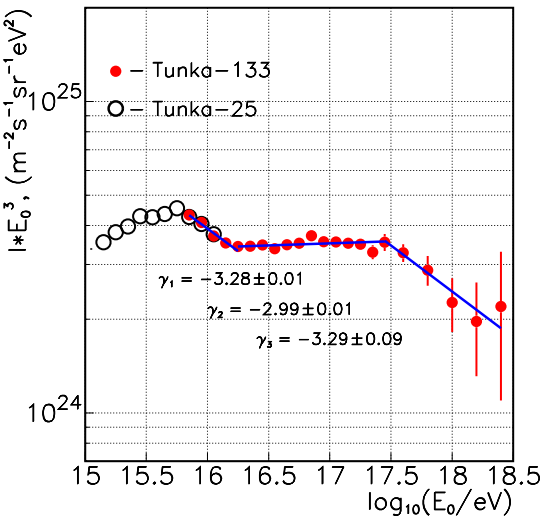

Fig. 16. Differential primary cosmic-ray energy spectrum with a fit of a doubly broken power law.

5.2. *Features in the energy spectrum*

The spectrum of Tunka-133 shows a number of features, that is deviations from a single power law. A power law applies only for spectral regions extending over less than half an order of magnitude. A fit with a doubly broken power law is shown in Fig. 16. At an energy of about $2 \cdot 10^{16}$ eV, the power law index changes from $\gamma = 3.28 \pm 0.01$ to $\gamma = 2.99 \pm 0.01$.

Table 1
All- particle energy spectrum.

$\log(E/eV)$	N_{events}	$dI/dE \pm stat \pm sys (m^{-2} sr^{-1} s^{-1} eV^{-1})$
15.85	70199	$(1.219 \pm 0.005 \pm 0.261) \times 10{-}23$
15.95	41904	$(5.780 \pm 0.028 \pm 1.238) \times 10{-}24$
16.05	53109	$(2.621 \pm 0.011 \pm 0.579) \times 10{-}24$
16.15	31788	$(1.246 \pm 0.070 \pm 0.262) \times 10{-}24$
16.25	19546	$(6.086 \pm 0.044 \pm 1.289) \times 10{-}25$
16.35	12363	$(3.058 \pm 0.026 \pm 0.614) \times 10{-}25$
16.45	7879	$(1.548 \pm 0.017 \pm 0.323) \times 10{-}25$
16.55	4830	$(7.537 \pm 0.011 \pm 1.762) \times 10{-}26$
16.65	3142	$(3.894 \pm 0.069 \pm 0.779) \times 10{-}26$
16.75	2004	$(1.973 \pm 0.044 \pm 0.446) \times 10{-}26$
16.85	1337	$(1.046 \pm 0.029 \pm 0.216) \times 10{-}26$
16.95	806	$(5.007 \pm 0.176 \pm 1.224) \times 10{-}27$
17.05	1604	$(2.504 \pm 0.063 \pm 0.682) \times 10{-}27$
17.15	1004	$(1.245 \pm 0.039 \pm 0.338) \times 10{-}27$
17.25	629	$(6.197 \pm 0.247 \pm 1.616) \times 10{-}28$
17.35	374	$(2.927 \pm 0.151 \pm 0.696) \times 10{-}28$
17.45	254	$(1.579 \pm 0.099 \pm 0.423) \times 10{-}28$
17.60	237	$(5.180 \pm 0.336 \pm 1.639) \times 10{-}29$
17.80	83	$(1.144 \pm 0.127 \pm 0.303) \times 10{-}29$
18.00	26	$(2.262 \pm 0.444 \pm 1.000) \times 10{-}30$
18.20	9	$(4.941 \pm 1.647 \pm 1.647) \times 10{-}31$
18.40	4	$(1.386 \pm 0.693 \pm 0.314) \times 10{-}31$

This feature was first observed by the KASCADE-Grande experiment [15]. The index can well be used up to $E_0 = 3 \cdot 10^{17}$ eV. But the statistical probability of a single power law representation in this energy range is rather small (about 3%). The main reason of this is one point at $\sim 7 \cdot 10^{16}$ eV, which is higher than the power law by about 2 standard deviations. This can be seen better if the y-axis is expanded as in Fig. 17. A similar feature at the same energy was observed in the experiment GAMMA [17].

The spectrum becomes much steeper with $\gamma = 3.29 \pm 0.09$ above $3 \cdot 10^{17}$ eV (the second "knee").

5.3. *Discussion*

In Fig. 18 the spectrum is compared to results from other experiments. The spectra of all the experiments shown in Fig. 18 – KASCADE [18], EAS-

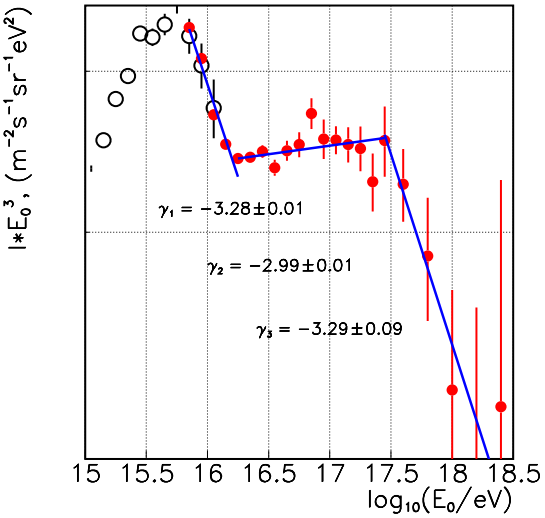

Fig. 17. Representation of the energy spectrum with an expanded scale of the y-axis.

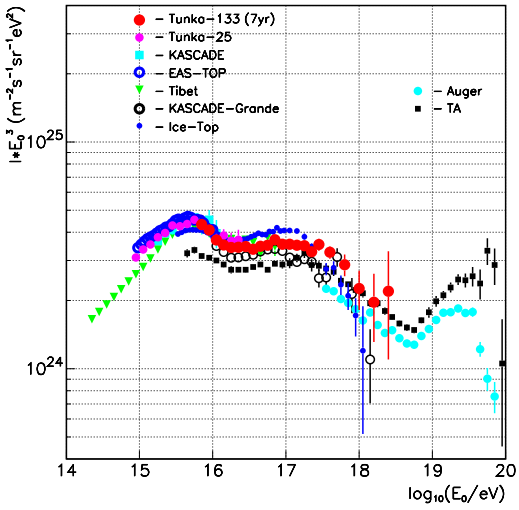

Fig. 18. Comparison of energy spectra obtained at the Tunka site to other experimental results.

TOP [16], Tibet [19], IceTop [20] – are practically indistinguishable at the energy of the first (classical) knee.

There is agreement between the spectra of Tunka-133, KASCADE-Grande [15] and IceTop [20] in the intermediate energy range $10^{16} - 10^{17}$ eV. We note that the difference between Tunka-133 and KASCADE-Grande spectra at E_0 about 10^{17} eV can be eliminated by an energy correction of only 4%. The energy shift between Tunka-133 data and IceTop data is slightly larger (about 7%). However, these shifts are smaller than the systematic errors of energy reconstruction in these experiments. The surprisingly good agreement among the spectra was emphasized in [22] and [21].

The paper [21] is devoted to the comparison of energy scales of Tunka-133 and KASCADE-Grande. The spectra were not only compared w.r.t. their form, but the absolute scales of both experiments have been compared via the radio extensions of these experiments named Tunka-Rex and LOPES. The radio detectors have been independently and accurately calibrated. The estimation of the absolute energy calibration uncertainty is less than 10% [21].

For highest energies the Tunka-133 data are in agreement with data from the Telescope Array (TA) [10] and the Pierre Auger Observatory [11], but naturally the Tunka-133 statistics is rather low above 10^{18} eV.

To get more statistics at this energy range, the scintillation counter array Tunka-Grande is presently being constructed at the Tunka-133 site[23]. The total data taking time will be 20 times higher than for the Cherenkov light array. The scintillation detectors will provide information on the number of electrons and muons in the EAS.

6. Conclusion

1. The primary CR energy spectrum in the range of $6 \cdot 10^{15} - 10^{18}$ eV has a number of features: the spectrum becomes harder (the index changes from $\gamma = 3.28 \pm 0.01$ to $\gamma = 2.99 \pm 0.01$) at $E_0 = 2 \cdot 10^{16}$ eV and steeper ($\gamma = 3.29 \pm 0.09$) at $E_0 = 3 \cdot 10^{17}$ eV.

2. In the energy range of $10^{16} - 10^{17}$ eV, the observed spectrum is consistent with spectra of KASCADE-Grande [15] and IceTop [20].

3. Beyond the energy of 10^{17} eV, the Tunka-133 spectrum is consistent with those from the Telescope Array [10] and the Pierre Auger Observatory [11].

7. Acknowledgment

This work is supported by the Russian Federation Ministry of Science and High Education (agreement: 075-15-2019-1631), the Russian Science Foundation (grant 19-72-20067 (section 5), grant 19-72-20230 (section 4)), the Russian Foundation for Basic Research (grants 19-52-44002, 16-29-13035).

References

[1] A.R. Bell, Astropart. Phys. 43 (2013) 56-70.
[2] P. Blasi, Comptes Rendus-Physique, 15 (2014) 329-338.
[3] F. Berezhnev et al. (Tunka Collaboration), Nucl. Instr. and Meth. A 692 (2012) 98-105.
[4] B. Antokhonov et al. (Tunka Collaboration), Nuclear Physics B (Proc.Suppl) 212-213 (2011) 247-252.
[5] D. V. Chernov et al. Int.J.Mod Phys. A20 (2005) 6796-6798.
[6] N. Budnev et al. Astropart. Phys. 50 (2013) 18-25.
[7] R. V. Vasiliev et al., Instr. and Exp. Tech., 52, № 2, (2009) 166-172.
[8] V. V. Prosin et al., Nucl. Instr. Methods Phys. Res. A 756 (2014) 94.
[9] V. V. Prosin for the Tunka Collaboration, Nuclear Physics B (Proc.Suppl) 190 (2009) 247-252
[10] T. Abu-Zayyad et al. Astropart. Phys. 48 (2013) 16
[11] A. Schulz for the Pierre Auger Collaboration, Proc. 33rd ICRC Rio De Janeiro (2013) ID=769
[12] E. Korosteleva et al. Int.J.Mod Phys. A20 (2005) 6837-6839, arXiv: astro-ph/0411216
[13] E. E. Korosteleva et al. Nuclear Physics B (Proc. Supp.) 165 (2007) 74-80
[14] A. Karle et al. Astropart. Phys. 3 (1995) 321
[15] W. D. Apel et al. (KASCADE-Grande Collaboration), Astropart. Phys. 36 (2012) 183
[16] M. Aglietta et al. EAS-TOP Collaboration, Astropart. Phys. 10 (1999) 1
[17] A. P. Garyaka et al. Journal of Physics G: Nuclear and Particle Physics 35 (2008) 115201
[18] T. Antony et al. Nucl. Instr. and Methods in Physics Research A 513 (2003) 490
[19] M. Amenomori et al. (Tibet Collaboration), Astrophys. J. 678 (2008) 1165
[20] Aartsen M.G., et al., Phys. Rev. Lett. D 88 (2013) 042004
[21] W. D. Apel et al. Physics Letters B 763 (2016) 179
[22] A. Haungs, Physics Procedia 00 (2015) 1-10
[23] R. D. Monkhoev et al. Journal of Instrumentation 12 6 (2017) 19